

Article

# First-Principles Study of Bimetallic Pairs Embedded on Graphene Co-Doped with N and O for N<sub>2</sub> Electroreduction

Haozhe Dong, Hao Sun, Guanru Xing, Shize Liu, Xuemei Duan \* and Jingyao Liu \* 

Institute of Theoretical Chemistry, College of Chemistry, Jilin University, Changchun 130023, China; donghz21@mails.jlu.edu.cn (H.D.); haosun22@mails.jlu.edu.cn (H.S.); xinggr21@mails.jlu.edu.cn (G.X.); szliu\_0520@163.com (S.L.)

\* Correspondence: duanxm@jlu.edu.cn (X.D.); lji121@jlu.edu.cn (J.L.)

**Abstract:** The electrocatalytic nitrogen reduction reaction (NRR) is considered a viable alternative to the Haber–Bosch process for ammonia synthesis, and the design of highly active and selective catalysts is crucial for the industrialization of the NRR. Dual-atom catalysts (DACs) with dual active sites offer flexible active sites and synergistic effects between atoms, providing more possibilities for the tuning of catalytic performance. In this study, we designed 48 graphene-based DACs with N<sub>4</sub>O<sub>2</sub> coordination (MM'@N<sub>4</sub>O<sub>2</sub>-G) using density functional theory. Through a series of screening strategies, we explored the reaction mechanisms of the NRR for eight catalysts in depth and revealed the “acceptance–donation” mechanism between the active sites and the N<sub>2</sub> molecules through electronic structure analysis. The study found that the limiting potential of the catalysts exhibited a volcano-shaped relationship with the d-band center of the active sites, indicating that the synergistic effect between the bimetallic components can regulate the d-band center position of the active metal M, thereby controlling the reaction activity. Furthermore, we investigated the selectivity of the eight DACs and identified five potential NRR catalysts. Among them, MoCo@N<sub>4</sub>O<sub>2</sub>-G showed the best NRR performance, with a limiting potential of −0.20 V. This study provides theoretical insights for the design and development of efficient NRR electrocatalysts.

**Keywords:** electrocatalytic nitrogen reduction reaction; dual-atom catalysts; density functional theory



**Citation:** Dong, H.; Sun, H.; Xing, G.; Liu, S.; Duan, X.; Liu, J. First-Principles Study of Bimetallic Pairs Embedded on Graphene Co-Doped with N and O for N<sub>2</sub> Electroreduction. *Molecules* **2024**, *29*, 779. <https://doi.org/10.3390/molecules29040779>

Academic Editors: Jalal Ghilane and Frantisek Hartl

Received: 22 December 2023

Revised: 25 January 2024

Accepted: 2 February 2024

Published: 8 February 2024



**Copyright:** © 2024 by the authors. Licensee MDPI, Basel, Switzerland. This article is an open access article distributed under the terms and conditions of the Creative Commons Attribution (CC BY) license (<https://creativecommons.org/licenses/by/4.0/>).

## 1. Introduction

Ammonia (NH<sub>3</sub>) is a key precursor in fertilizer synthesis and a carbon-free energy carrier that possesses advantages such as emission-free combustion, convenient storage, and high energy density. Its role in sustainable development is crucial [1–3]. However, current industrial ammonia production heavily relies on the energy-intensive Haber–Bosch process, requiring high temperatures and pressure (300–500 °C, 150–300 atm) for NH<sub>3</sub> synthesis [4]. This process not only consumes a notable amount of energy (approximately 1–2% of global energy consumption annually), but also releases substantial greenhouse gases. As a result, there is an urgent need to explore sustainable alternatives [5]. Electrocatalytic nitrogen reduction (eNRR) has emerged as a promising alternative method due to its mild reaction conditions, sustainability, and environmental friendliness, potentially replacing the conventional Haber–Bosch process [6]. However, the activation of N<sub>2</sub> molecules faces challenges due to the high bond energy of the N≡N bond (941 kJ·mol<sup>−1</sup>), low polarizability, and lack of a dipole moment [7]. Consequently, NRR catalysis often requires a high limiting voltage to overcome these obstacles. Additionally, the simultaneous hydrogen evolution reaction (HER) during eNRR compromises the NH<sub>3</sub> selectivity and Faradaic efficiency (FE) [8]. Thus, the focus lies in developing electrocatalysts with outstanding catalytic activity, high selectivity, and superior FE for large-scale industrial eNRR applications.

In recent years, atomically dispersed transition metal (TM) catalysts, including single-atom catalysts (SACs) and dual-atom catalysts (DACs) have garnered substantial interest

in the field of catalysis due to their high atomic utilization, tunable electronic structures, and unique local chemical environments [9–12]. Currently, there have been a large number of computational and experimental studies on SACs for eNRR. In atomically dispersed transition metal catalysts, choosing suitable support materials is crucial to prevent metal agglomeration and enhance the catalyst stability [13–16]. Two-dimensional materials, such as graphene,  $C_2N$ ,  $g-C_3N_4$ ,  $h-BN$ , and MXene, have been commonly used as substrates for SACs or DACs owing to their large surface area, ordered structure, and controllable electronic properties. Among these, graphene stands out as an ideal substrate for SACs and DACs due to its high charge carrier mobility, excellent conductivity, and chemical stability [17–21]. Recently, special attention has been directed towards the family of transition metal atoms anchored on N-doped graphene ( $TM-N_x/G$ ), such as  $TM-N_4$  [22], due to its high reactivity and stability. However, they often exhibit lower overpotential in the hydrogen evolution reaction (HER), leading to lower Faradaic efficiency for the NRR. To address this issue, strategies involving the adjustment of active sites and/or coordination environments have been proposed to improve the catalytic performance and stability [23–25].

As an extension of SACs, DACs utilize the synergistic effect introduced by the second metal to maintain the low oxidation state of transition metals and effectively activate inert molecules [26]. Experimental and theoretical evidence indicates that some DACs, such as  $Mn_2@C_2N$  [27],  $FeM-N_6-C$  [28];  $Fe_2N_4@graphene$  [29],  $FeRu@N_4-P$  [30], and  $Mo_2@PC_6$  [31], exhibit superior catalytic performance in eNRR compared to Ru (0001) ( $-0.98$  V) [32]. Nevertheless, the stability and catalytic performance of these catalysts are highly sensitive to the coordination environment of the metal centers [33]. Previous studies have demonstrated that adjusting the atoms in the first coordination layer around the transition metal atoms is an effective strategy to modulate the catalytic performance. In  $TM-N_x/G$ , the introduction of additional non-metallic dopants (such as oxygen, boron, sulfur, etc.) in the first coordination layer around the transition metal atom significantly enhances the catalytic performance beyond N atom coordination alone [34–36]. For instance, in the  $M_2N_6/G$  system, the  $Mn_2$  diatomic catalyst with O and N co-coordination ( $Mn_2ON_5/G^\alpha$ ) demonstrates significantly improved NRR activity and selectivity [37]. In addition, by employing different transition metals and ligands, DACs have the potential to break linear proportionality in certain reactions [38]. DACs exhibit promising prospects in eNRR applications due to the ability to flexibly choose different metal combinations and coordination environments, and the number of active centers.

A recent experimental approach demonstrated a synthetic method to produce a library of DACs using macrocyclic precursors through an encapsulation–thermal decomposition synthesis strategy. This led to the successful synthesis of a series of nitrogen and oxygen co-doped porous carbon-supported DACs ( $MM'@N_4O_2-G$ ) [39]. These complexes allow for a wide range of metal center modulation, including 3d transition metals (Mn, Fe, Co, Ni, Cu, Zn) and noble metals (Pd, Rh, Pt). Furthermore, by independently controlling elements, the formation of both homonuclear and heteronuclear bimetallic centers, such as  $Fe_2$ ,  $Co_2$ ,  $FeCu$ , and  $CuCo$ , can be achieved. The study revealed that these DACs exhibit excellent catalytic activity and stability in the oxygen reduction reaction (ORR), particularly with  $FeCu$ -DAC outperforming corresponding SACs and other Fe-based DACs. This progress has inspired us to design dual-atom catalysts with diverse metal combinations and  $N_4O_2$  coordination for the NRR.

In this study, we employed density functional theory (DFT) to investigate the catalytic performance of a series of DACs with the  $M_2N_4O_2$  motif embedded in graphene ( $MM'@N_4O_2-G$ ) for the NRR to  $NH_3$ . In terms of metal selection, considering the common metals found in the active centers of nitrogenase (such as Mo, V, and Fe) [36], we chose these three metals as M, while M' included 3d transition metals (Sc–Zn), 4d transition metals (Zr, Nb, and Mo), and 5d transition metals (Hf, Ta, W, and Re). The computational results indicate that these five DACs exhibit good catalytic performance for the NRR while inhibiting the side reaction (HER). Detailed analysis of the electronic structure properties of these catalysts revealed that the high activity of the DACs stemmed from the effective

modulation of the intermediate stability and synergistic effects between the active sites. This study is anticipated to offer an important reference and guidance for the development of highly active and selective DACs.

## 2. Results and Discussion

### 2.1. Catalyst Structure and Stability

Based on the successful synthesis of DACs possessing  $N_4O_2$  coordination in experiments, we constructed 48 types of  $MM'@N_4O_2$ -G DACs on this substrate, including 3 homonuclear DACs, VV/MoMo/FeFe@ $N_4O_2$ -G, and 45 heteronuclear DACs,  $MM'@N_4O_2$ -G, where  $M = V/Fe/Mo$  and  $M' = Sc \sim Zn, Zr, Nb, Mo, Hf, Ta, W,$  and  $Re$ . The optimized structures are shown in Figure 1a. To assess the thermodynamic stability of these catalysts, we calculated the formation energy ( $E_f$ ) as follows:

$$E_f = (E_{cat} - E_{sub} - E_M - E_{M'})$$

where  $E_{cat}$  is the total energy of the optimized catalyst,  $E_{sub}$  is the energy of the catalyst substrate, and  $E_M$  is the energy of an individual metal atom in its most stable bulk phase structure. Subsequently, we calculated the dissolution potential ( $U_{diss}$ ) to evaluate the electrochemical stability:

$$U_{diss} = U_{diss}^0 - E_f/N_e$$

where  $U_{diss}$  represents the standard dissolution potential of the bulk metal, denoted as  $U_{diss}^0 = [U_{diss}^0(M) + U_{diss}^0(M')]/2$  for the diatomic system;  $N_e$  represents the number of electrons transferred during metal dissolution, expressed as  $N_e = [N_e(M) + N_e(M')]/2$  [28]. According to the calculated results shown in Figure 1b, the  $E_f$  values of these catalysts are all negative, indicating their thermodynamic stability. Moreover, among the 48 diatomic catalysts, 33 exhibit  $U_{diss}$  values greater than 0, indicating good electrochemical stability while maintaining thermodynamic stability. Consequently, they are potential candidate catalysts for further investigation. Additionally, Bader charge analysis was used to calculate the charge transfer between the anchored metal atoms and the substrate. As shown in Table S1, a substantial number of electrons transfer from the anchored metal atoms to  $N_4O_2$ -G, indicating a strong interaction between the metal and the substrate.

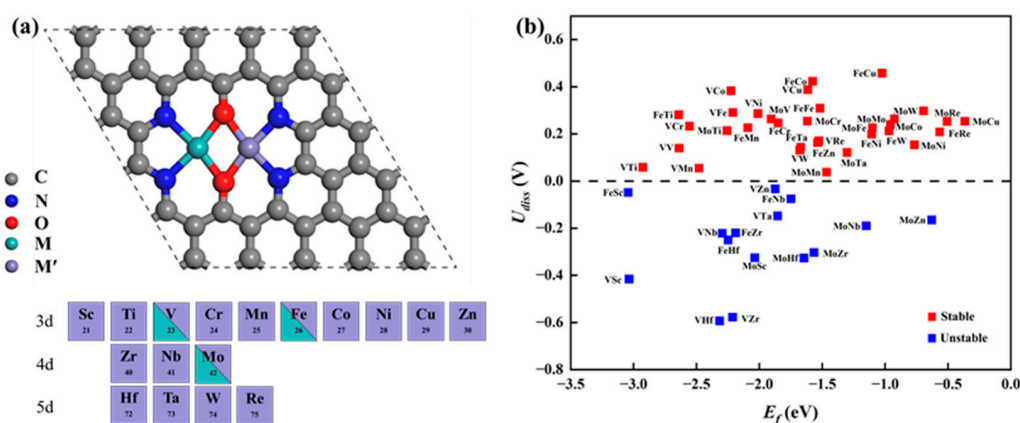


**Figure 1.** (a) Schematic of the optimized catalyst structure. (b) Corresponding formation energy and dissolution potential of the catalyst.

### 2.2. Performance of $MM'@N_4O_2$ -G for Electrocatalytic NRR

#### 2.2.1. Screening of Catalysts

$N_2$  adsorption. The adsorption and activation of  $N_2$  molecules represent the initial and crucial steps in the NRR process. To determine the most favorable adsorption structures, three types of adsorption configurations were considered for homonuclear DACs: one involving end-on adsorption, where one N atom of  $N_2$  forms a bond with a single metal

atom, and two types of side-on adsorption, one with two N atoms of  $N_2$  adsorbed on a single metal atom and the other with two N atoms of  $N_2$  bonded to two different metal atoms. Regarding heteronuclear DACs, given the diverse nature of the two metal active sites, five adsorption configurations were considered, comprising two end-on adsorptions and three side-on adsorptions, as shown in Figure 2a. Figure 2b presents the adsorption free energy ( $\Delta G_{*N_2}$ ) of the optimized  $N_2$  adsorption configurations on 33 catalysts. Notably, except for the physical adsorption of  $N_2$  molecules on four catalysts (MM'@N<sub>4</sub>O<sub>2</sub>-G, MM' = FeTa, FeMn, FeCo, and FeNi), the other 29 catalysts demonstrate the chemical adsorption of  $N_2$  molecules on the surface, with adsorption free energy values ranging from  $-0.06$  to  $-1.07$  eV. Among them,  $N_2$  molecules exhibit side-on adsorption on four catalysts (MM'@N<sub>4</sub>O<sub>2</sub>-G, MM' = VV, VTi, MoTa, and MoTi), while end-on adsorption is mainly observed on 25 other catalysts, mainly at the M or M' active sites of MM'@N<sub>4</sub>O<sub>2</sub>-G. Thus, based on the calculated adsorption free energy of  $N_2$ , only four catalysts (MM'@N<sub>4</sub>O<sub>2</sub>-G, MM' = FeTa, FeMn, FeCo, and FeNi) are excluded.

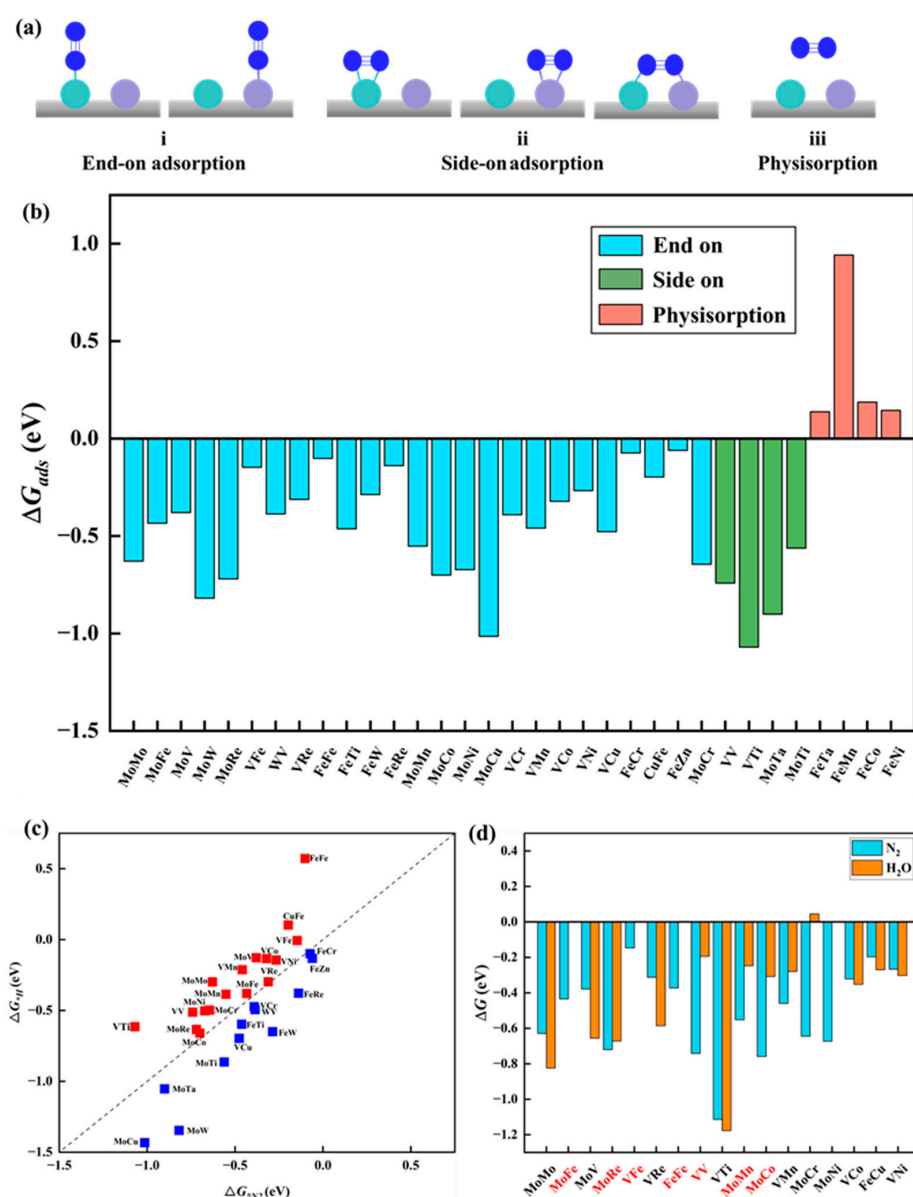


**Figure 2.** (a) Schematic structure of  $N_2$  adsorption on catalyst. (b) The adsorption free energy of  $N_2$  on the catalyst. (c) Comparison between  $\Delta G_{*H}$  and  $\Delta G_{*N_2}$ . (d) Comparison between  $\Delta G_{*N_2}$  and  $\Delta G_{*H_2O}$ , where the red coordinates represent the catalysts that meet the requirements.

Competitive adsorption at active sites. In the NRR, competitive adsorption among different species at active sites is an important concern, especially under experimental conditions where hydrogen protons and water molecules in the solution may compete for adsorption with  $N_2$  molecules at the active sites on the catalyst surface. If the catalyst exhibits stronger adsorption of hydrogen atoms compared to  $N_2$  molecules, this could potentially lead to the occupation of active sites by hydrogen atoms, favoring the promotion of the HER over the NRR. Such a case leads to the decreased Faradaic efficiency of the NRR, thereby impacting the selectivity and efficiency of the overall reaction. To evaluate this, we compared the adsorption free energies of  $*H$  ( $\Delta G_{*H}$ ) and  $\Delta G_{*N_2}$ . Figure 2c illustrates that 17 catalysts exhibit stronger adsorption towards  $N_2$  molecules than towards H atoms, indicating that these catalysts are more conducive to facilitating an efficient electrochemical NRR. Additionally, if solvent molecules cover metal atoms instead of  $N_2$  molecules, it can affect the sustained NRR and lead to the oxidation of transition metals in the aqueous electrolyte, ultimately hindering the progress of the reaction [40]. To address this issue, the adsorption free energy of  $H_2O$  molecules ( $\Delta G_{*H_2O}$ ) on the remaining 17 catalysts was calculated, as shown in Figure 3d. Ten  $MM'@N_4O_2-G$  catalysts ( $MM' = MoFe, MoRe, VFe, FeFe, VV, MoMn, MoCo, VMn, MoCr, MoNi$ ) were identified for their favorable adsorption behavior towards  $N_2$  molecules within the competitive adsorption environment. These catalysts show promising potential for an efficient NRR.

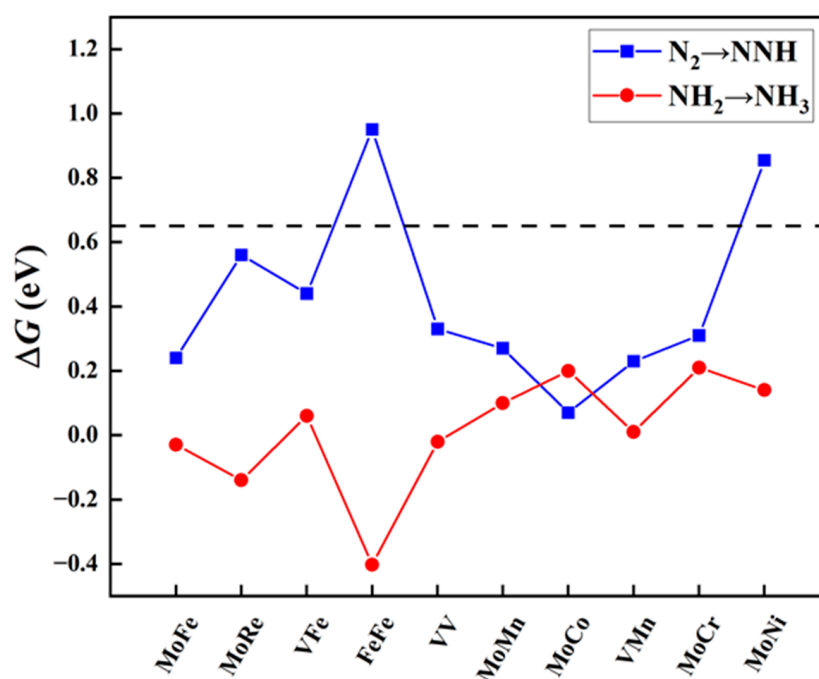


**Figure 3.** Free energy changes ( $\Delta G_{N_2 \rightarrow NNH}$  and  $\Delta G_{NH_2 \rightarrow NH_3}$ , eV) for the first and last protonation steps on  $MM'@N_4O_2-G$ . The black dashed line indicates the screening criteria ( $\Delta G = 0.65$  eV).

The protonation of the first step and the last step. The eNRR involves six proton-coupled electron transfer (PCET) steps. Despite the specific mechanism of the NRR, the hydrogenation reactions of the first step ( $*N_2 + H^+ + e^- \rightarrow *NNH$ ) and the sixth step ( $*NH_2 + H^+ + e^- \rightarrow *NH_3$ ) are the most common elementary steps. Previous studies have indicated [41–43] that these two steps usually act as the potential determining steps (PDS) in the NRR, demonstrating the largest free energy change throughout the reaction process. To evaluate these crucial steps, we calculated the reaction free energy change for the protonation of the first step ( $\Delta G_{N_2 \rightarrow NNH}$ ) and the last step ( $\Delta G_{NH_2 \rightarrow NH_3}$ ). Using a standard value of 0.65 eV, we performed preliminary screening for the aforementioned ten candidate diatomic catalysts. As shown in Figure 3, eight catalysts met the criteria set in this study, including one homonuclear DAC ( $VV@N_4O_2-G$ ) and seven heteronuclear DACs

( $MM'@N_4O_2-G$ ,  $MM' = MoCo, MoFe, MoCr, MoMn, MoRe, VFe,$  and  $VMn$ ). Additionally, it is notable that, for most diatomic catalysts, the free energy change for the protonation of  $N_2$  to form  $NNH$  in the first step is greater, except for  $MoCo@N_4O_2-G$ , where the  $\Delta G_{NH_2 \rightarrow NH_3}$  (0.20 eV) is greater compared to  $\Delta G_{N_2 \rightarrow NNH}$  (0.07 eV).

**Thermal stability of the catalyst.** The stability of catalysts under operating conditions is crucial for their practical application. To further assess the thermal stability of the 8 catalysts, we conducted a 10 ps ab initio molecular dynamics (AIMD) simulation at a temperature of 500 K. Figure 4 and Figure S1 illustrate the variations in temperature and energy over time for these catalysts. Clearly, during the 10 ps duration, there were negligible structural changes observed in the catalysts, indicating excellent thermal stability.

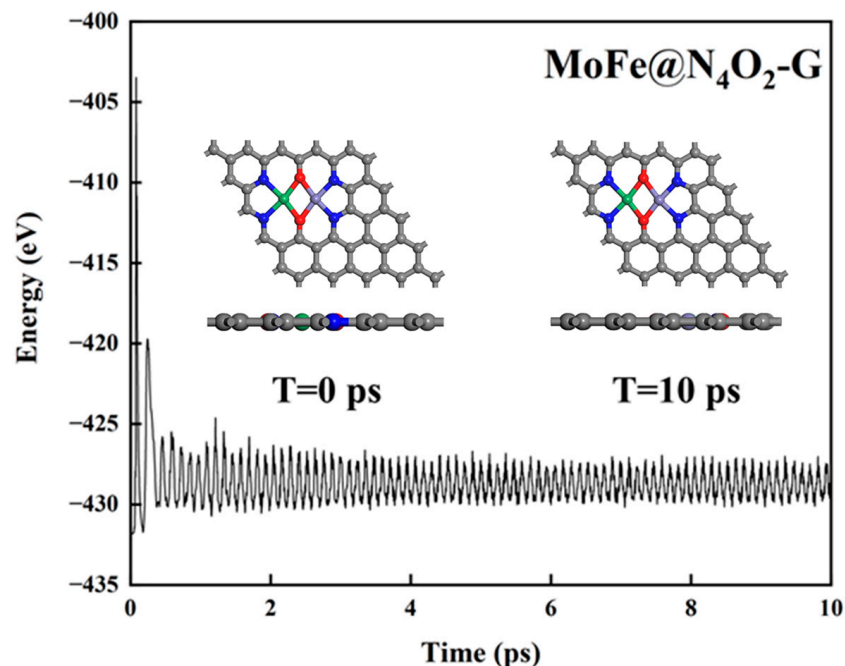


**Figure 4.** Total energy variation of  $MoFe@N_4O_2-G$  for AIMD simulation at 500 K for 10 ps. The C, N, O, Mo, and Fe atoms are labeled as gray, blue, red, green, and lavender balls, respectively.

### 2.2.2. NRR Reaction Mechanism

For the eight DACs selected through the aforementioned screening process, we conducted detailed calculations of the possible NRR pathways to assess their catalytic performance. Based on the  $N_2$  adsorption configurations and different hydrogenation sequences of the two N atoms, the electrocatalytic NRR on DAC surfaces typically involves various pathways, as shown in Figure 5. For  $N_2$  adsorption through the end-on pattern, the NRR can proceed via either distal or alternating pathways for protonation reactions. In the distal pathway, the proton–electron pairs initially react with the N atom away from the adsorption site, resulting in the formation of the first  $NH_3$ . Subsequently, consecutive protonation steps lead to the formation of the second  $NH_3$ . In the alternating pathway, the proton–electron pairs alternately attack the two N atoms, eventually leading to the sequential production of two  $NH_3$  molecules. Regarding the side-on adsorption pattern, the NRR occurs via two pathways: the enzymatic (red line) and the consecutive pathways (brown line). Additionally, the NRR can also take place through a mixed pathway, alternating between the distal and alternating pathways or between the enzymatic and consecutive pathways.

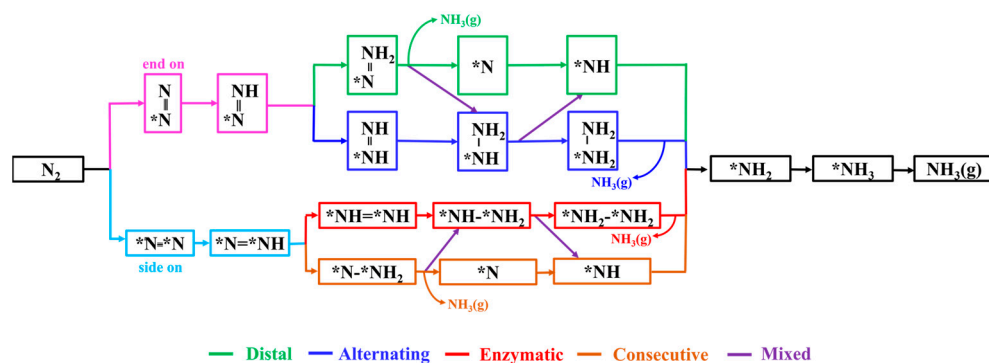


Figure 5. Diagram of possible reaction mechanisms for NRR.

VV@N<sub>4</sub>O<sub>2</sub>-G was the only homonuclear DAC that remained after the screening process. N<sub>2</sub> molecules exhibit side-on adsorption on the catalyst surface, where two N atoms bond to two V atoms, with  $\Delta G_{*N_2}$  of  $-0.76$  eV. The Gibbs free energy diagram for the NRR on VV@N<sub>4</sub>O<sub>2</sub>-G and corresponding intermediate structures are shown in Figure 6. As shown in the figure, for the VV@N<sub>4</sub>O<sub>2</sub>-G catalyst, the potential-determining step (PDS) in the consecutive pathway is the second step of the protonation reaction ( $*NNH + H^+ + e^- \rightarrow *NNH_2$ ), with a  $\Delta G$  value of  $0.49$  eV. The PDS of both the enzymatic and mixed pathways is the first protonation step ( $*N_2 + H^+ + e^- \rightarrow *NNH$ ), with a  $\Delta G$  value of  $0.32$  eV. The first four protonation steps in the two pathways lead to the  $*NHNH_2$  intermediate. In the fifth protonation step, a proton–electron pair attacks one N atom in the  $*NHNH_2$  intermediate, forming  $*NH_2NH_2$  or  $*NHNH_3$ , with  $\Delta G$  values of  $1.84$  and  $-1.35$  eV, respectively, indicating that the former is more feasible in thermodynamical terms. Subsequently,  $*NH_2 + *NH_2$  undergoes two hydrogenation steps to produce two adsorbed NH<sub>3</sub> molecules, with  $\Delta G$  values of  $0.02$  and  $-0.02$  eV. It is noteworthy that the desorption of the two NH<sub>3</sub> molecules from VV@N<sub>4</sub>O<sub>2</sub>-G requires relatively high energies, at  $1.34$  eV and  $0.82$  eV, respectively. However, previous studies have demonstrated that NH<sub>3</sub> generated in strong acid solutions can be easily reduced to NH<sub>4</sub><sup>+</sup> [44]; hence, the desorption of NH<sub>3</sub> is not extensively considered here. Our calculations show that for VV@N<sub>4</sub>O<sub>2</sub>-G, the most probable reaction pathway is the enzymatic pathway, with a  $U_L$  of  $-0.32$  V.

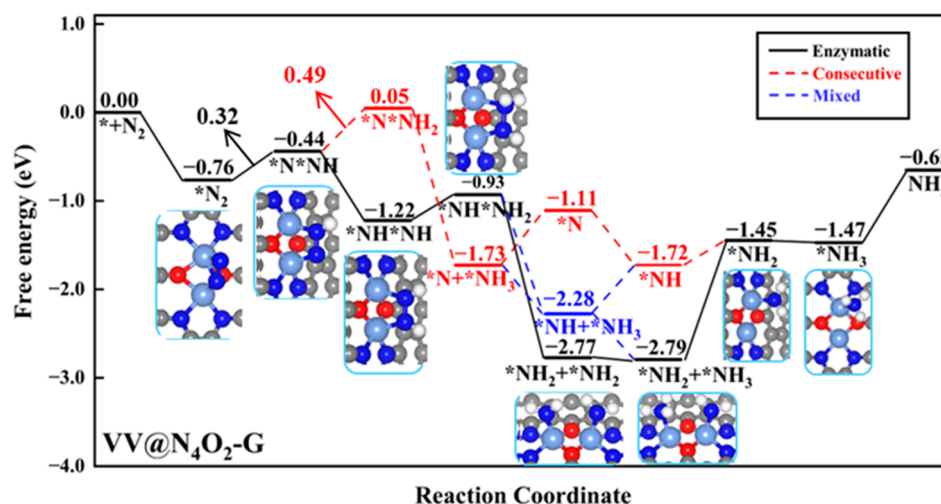
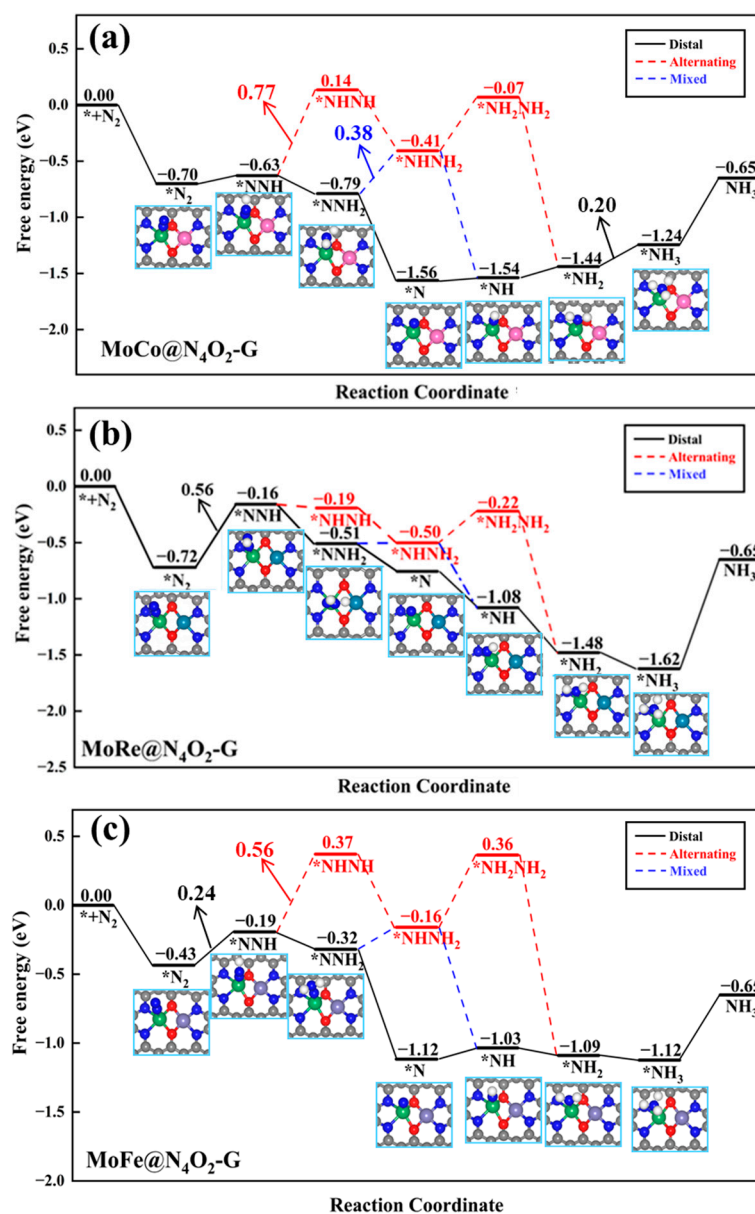


Figure 6. Gibbs free energy diagrams of NRR on VV@N<sub>4</sub>O<sub>2</sub>-G. The C, N, O, H, and V atoms are labeled as gray, blue, red, white, and light blue balls, respectively.

In the other seven heteronuclear DACs (MM'<sup>1</sup>@N<sub>4</sub>O<sub>2</sub>-G, MM'<sup>1</sup> = MoCo, MoCr, MoFe, MoMn, MoRe, VFe, and VMn), N<sub>2</sub> is adsorbed in an end-on configuration on Mo or V atoms. As depicted in Figure 7a, for the MoCo@N<sub>4</sub>O<sub>2</sub>-G catalyst, the protonation reactions follow

three different reaction pathways (distal, alternating, and mixed pathways) with the PDS as the sixth step ( $*\text{NH}_2 + \text{H}^+ + \text{e}^- \rightarrow *\text{NH}_3$ ), the second step ( $*\text{NNH} + \text{H}^+ + \text{e}^- \rightarrow *\text{NNH}_2$ ), and the third step ( $*\text{NNH}_2 + \text{H}^+ + \text{e}^- \rightarrow *\text{NHNH}_2$ ), with  $\Delta G$  values of 0.20 eV, 0.77 eV, and 0.38 eV, respectively. Consequently, the distal pathway becomes the most favorable reaction pathway for  $\text{MoCo@N}_4\text{O}_2\text{-G}$ . For  $\text{MoRe@N}_4\text{O}_2\text{-G}$  and  $\text{VFe@N}_4\text{O}_2\text{-G}$ , as shown in Figures 7b and S2, the PDS for all three pathways is the first protonation step, with  $\Delta G_{\text{max}}$  values of 0.56 and 0.44 eV, respectively. However, compared to the alternating and mixed pathways, the distal pathway displays superior thermodynamic advantages on these two catalysts. Therefore, the NRR on  $\text{MoRe@N}_4\text{O}_2\text{-G}$  and  $\text{VFe@N}_4\text{O}_2\text{-G}$  tends to proceed along the distal pathway. As for the remaining four DACs ( $\text{MoFe@N}_4\text{O}_2\text{-G}$ ,  $\text{MoCr@N}_4\text{O}_2\text{-G}$ ,  $\text{MoMn@N}_4\text{O}_2\text{-G}$ , and  $\text{VMn@N}_4\text{O}_2\text{-G}$ ), as depicted in Figures 7c and S3, all show a preference for the distal pathway in the NRR. The PDS is represented by  $*\text{NNH} + \text{H}^+ + \text{e}^- \rightarrow *\text{NNH}_2$ , with corresponding  $U_L$  values of  $-0.24$ ,  $-0.25$ ,  $-0.27$ , and  $-0.23$  eV, respectively.



**Figure 7.** Gibbs free energy diagrams of NRR on (a)  $\text{MoCo@N}_4\text{O}_2\text{-G}$ , (b)  $\text{MoRe@N}_4\text{O}_2\text{-G}$ , and (c)  $\text{MoFe@N}_4\text{O}_2\text{-G}$ . The C, N, O, H, Mo, Co, Re, and Fe atoms are labeled as gray, blue, red, white, green, pink, dark green, and lavender balls, respectively.

Due to the end-on adsorption of  $N_2$  on heteronuclear DACs, when a  $N_2$  molecule adsorbs on one metal atom and undergoes the NRR through a distal pathway, the other metal atom can also serve as a reactive site. We further investigated the NRR mechanism when two  $N_2$  molecules were simultaneously adsorbed on these seven heteronuclear DACs. Firstly, we studied the co-adsorption of two  $N_2$  molecules on the diatomic sites. It was found that the second  $N_2$  molecule only physisorbed on the catalyst surface in the cases of  $MoCr@N_4O_2-G$ ,  $VMn@N_4O_2-G$ ,  $VFe@N_4O_2-G$ , and  $MoMn@N_4O_2-G$ , while the adsorption free energies of the second  $N_2$  molecule on  $MoFe@N_4O_2-G$ ,  $MoRe@N_4O_2-G$ , and  $MoCo@N_4O_2-G$  were  $-0.34$ ,  $-0.69$ , and  $-0.41$  eV, respectively. Subsequently, we calculated the free energy changes from  $*N_2 + *N_2$  to  $*NNH + *N_2$  on the latter three catalysts. On  $MoFe$ ,  $MoRe$ , and  $MoCo$ , the free energy changes from  $*N_2 + *N_2$  to  $*NNH(Mo) + *N_2$  are  $0.32$ ,  $0.35$ , and  $0.32$  eV, respectively, while the free energy changes from  $*N_2 + *N_2$  to  $*N_2 + *NNH(M')$  are  $1.18$ ,  $1.76$ , and  $0.62$  eV, respectively. The results indicate that on the surfaces of  $MoFe@N_4O_2-G$  and  $MoCo@N_4O_2-G$ , the  $\Delta G$  of this step is larger than the rate-determining step's free energy obtained when a single  $N_2$  molecule is adsorbed, indicating that simultaneously adsorbing two  $N_2$  molecules is not feasible on these two surfaces (Table S2). Conversely, on the  $MoRe@N_4O_2-G$  surface, the  $\Delta G$  of this step is lower than the  $\Delta G_{max}$  when a single  $N_2$  is adsorbed, suggesting that the  $MoRe@N_4O_2-G$  catalyst can simultaneously adsorb two  $N_2$  molecules for the NRR, preferentially inducing the first hydrogenation of the  $N_2$  adsorbed on the Mo atom.

In the subsequent reaction processes, because both  $N_2$  molecules have the potential for hydrogenation, we compared the free energy changes of two hydrogenation elementary steps starting from the intermediate  $*NNH$ :  $*NNH + *N_2 \rightarrow *NNH + *NNH$  and  $*NNH + *N_2 \rightarrow *NNH_2 + *N_2$ . The former displays a much higher free energy change ( $1.11$  eV) compared to the latter ( $0.05$  eV). Similarly, for the two elementary steps starting from the intermediate  $*NNH_2$ , the  $\Delta G$  of  $*NNH_2 + *N_2 \rightarrow *NNH_2 + *NNH$  ( $1.14$  eV) is much higher than that of  $*NNH + *N_2 \rightarrow *NNH_2 + *N_2$ . Therefore, we infer that on  $MoRe@N_4O_2-G$ , the NRR continuously hydrogenates one  $N_2$  molecule while suppressing the hydrogenation of another  $N_2$  molecule. The corresponding reaction free energy diagram and optimized intermediate structures are depicted in Figure 8. Computational results indicate that the mixed pathway is the most feasible route and the PDS remains as  $*N + *N_2 + H^+ + e^- \rightarrow *NNH + *N_2$ , with a  $U_L$  of  $-0.35$  V, significantly lower than the  $U_L$  ( $-0.56$  V) corresponding to the case when a single  $N_2$  adsorbs on the surface. Consequently, it can be inferred that on  $MoRe@N_4O_2-G$ , the NRR is more inclined towards the adsorbing two  $N_2$  molecules and follows a mixed mechanism.

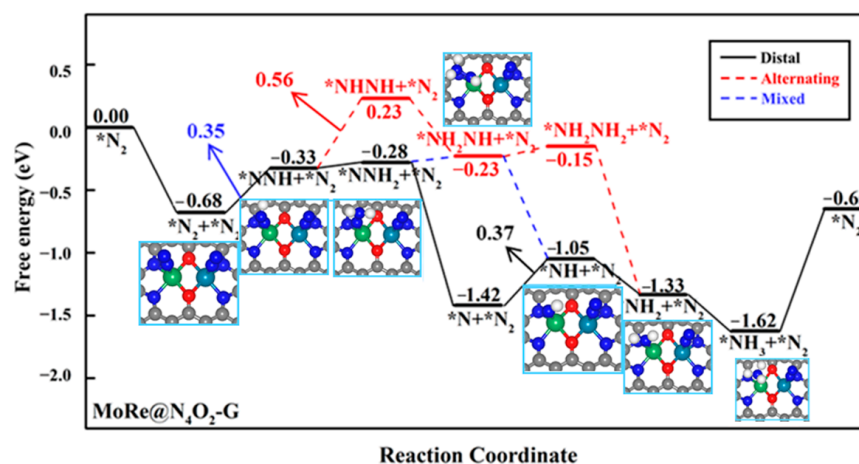


**Figure 8.** Gibbs free energy diagram of NRR on  $MoRe@N_4O_2-G$  adsorption of two  $N_2$  molecules. The C, N, O, H, Mo, and Re atoms are labeled as gray, blue, red, white, green, and dark green balls, respectively.

### 2.3. Origin of NRR Catalytic Activity

To investigate the underlying factors influencing the activity of DACs in the NRR, we conducted electronic structure calculations on these eight DACs. Firstly, we analyzed the charge transfer between the  $N_2$  molecule and the catalyst through charge density difference (CDD) and Bader charge analysis. Taking  $MoCo@N_4O_2$  as an example, as shown in Figure 9a, evident charge transfer between the active site and  $N_2$  is observed, with a tendency for charge accumulation near the proximal N atom of  $N_2$ , reducing the charge density between the two N atoms, thereby weakening the chemical bond and facilitating  $N_2$  activation. Additionally, the increased N-N bond length after  $N_2$  adsorption also reflects the activation of  $N_2$ . Compared to free  $N_2$  molecules ( $d_{N-N} = 1.114 \text{ \AA}$ ), the adsorbed  $N_2$  exhibits a significantly increased N-N bond length, ranging from  $1.148 \text{ \AA}$  to  $1.269 \text{ \AA}$ , indicating that the electron transfer between the catalyst and  $N_2$  effectively activates the  $N_2$  molecule.

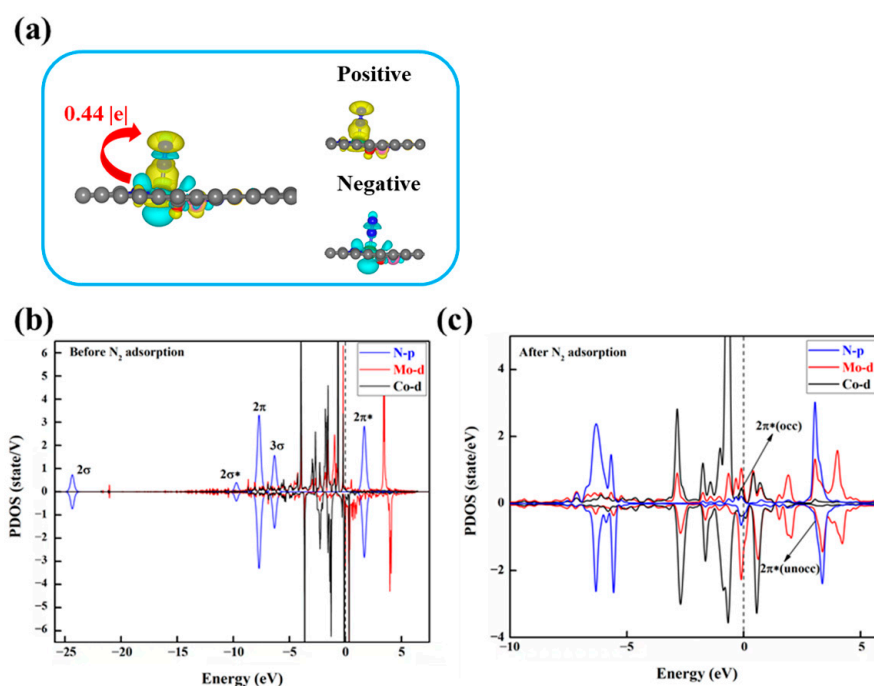


**Figure 9.** (a) Charge density differences after  $N_2$  adsorption on  $MoCo@N_4O_2-G$  and Bader charge ( $Q_{*N_2}$ , |e|) after  $N_2$  adsorption. The C, N, O, Mo, and Co atoms are labeled as gray, blue, red, green, and pink balls, respectively. The electrons accumulation and loss are represented by yellow and cyan areas. (b) PDOS before and (c) after  $N_2$  adsorption on  $MoCo@N_4O_2-G$ . The black dashed line represents the Fermi energy level.

In order to gain deeper insights into the fundamental electron transfer mechanism during  $N_2$  activation, using  $MoCo@N_4O_2-G$  as an example, the partial density of states (PDOS) of the DACs before and after  $N_2$  adsorption was studied, as shown in Figure 9b,c. Compared to the free  $N_2$  molecular orbitals, the  $2\pi$  and  $3\sigma$  orbitals of the adsorbed  $N_2$  shift upwards and exhibit significant hybridization with the Mo 3d orbitals below the Fermi level. This indicates that the unoccupied 3d orbitals of the Mo atom accept electrons from the  $2\pi$  and  $3\sigma$  orbitals of the  $N_2$  molecule, forming bonding states that promote nitrogen adsorption. On the other hand, the unoccupied  $2\pi^*$  orbitals of  $N_2$  move towards the Fermi level after adsorption, forming partially occupied  $2\pi^*$  orbitals. This suggests that the occupied 3d orbitals of the Mo atom donate electrons to the antibonding orbitals of  $N_2$ , thereby weakening the strength of the N-N bond and facilitating subsequent hydrogenation reactions. Similar situations are observed in the PDOS of other DACs (Figure S4), indicating that  $N_2$  activation on these catalysts follows an “acceptance–donation” mechanism.

Moreover, to investigate the mechanism of the synergistic effects between diatomic sites, we explored the influence of the d-band center ( $\epsilon_d$ ) of the active sites on the reac-

tion activity. Specifically, we evaluated the d-band center of the Mo atom in the case of MoCo@N<sub>4</sub>O<sub>2</sub>-G and assessed the d-band center of the two V atoms in VV@N<sub>4</sub>O<sub>2</sub>-G. As shown in Figure 10, a distinct volcano-shaped relationship exists between the limiting potentials of these eight DACs and the d-band centers of the active metal atoms. Notably, the highly efficient MoCo@N<sub>4</sub>O<sub>2</sub>-G is located near the peak of the volcano plot. The volcano curve suggests that the superior NRR performance of DACs is attributed to the appropriate position of the d-band center. Additionally, it is evident that although the metal M' (in the case of heteronuclear DAC) does not directly participate in the hydrogenation process of N<sub>2</sub>, the synergistic effects between the M' and M sites effectively regulate the position of the d-band center of the active site, thereby impacting the reaction activity.

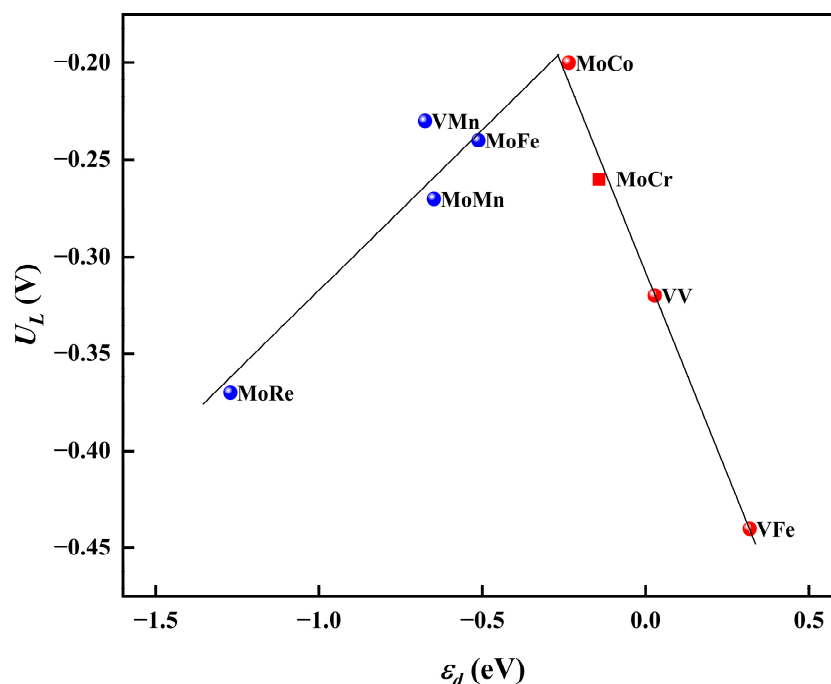


**Figure 10.** Relationship between  $U_L$  and  $\epsilon_d$  on  $MM'@N_4O_2-G$ .

#### 2.4. NRR Selectivity of the $MM'@N_4O_2-G$ Catalysts

The main competing reaction during the NRR is the HER. This competition greatly influences the selectivity of the catalyst. The difference between  $U_L(\text{NRR})$  and  $U_L(\text{HER})$  is commonly used to assess the selectivity of a catalyst. A positive value of  $U_L(\text{NRR}) - U_L(\text{HER})$  indicates that the catalyst favors the NRR over the HER, while a negative value indicates the opposite. The results of  $U_L(\text{NRR}) - U_L(\text{HER})$  of eight DACs are shown in Figure 11. It can be seen that MoRe@N<sub>4</sub>O<sub>2</sub>-G, VMn@N<sub>4</sub>O<sub>2</sub>-G, and VFe@N<sub>4</sub>O<sub>2</sub>-G exhibit negative  $U_L(\text{NRR}) - U_L(\text{HER})$  values, indicating poor selectivity for the NRR. Conversely, the remaining five catalysts ( $MM'@N_4O_2-G$ ,  $MM' = \text{MoFe, MoMn, MoCo, MoCr, and VV}$ ) all have positive values for  $U_L(\text{NRR}) - U_L(\text{HER})$ . Notably, because four ( $MM'@N_4O_2-G$ ,  $MM' = \text{MoFe, MoMn, MoCo, and MoCr}$ ) of these five catalysts adsorb N<sub>2</sub> onto their surfaces via an end-on mode, the initial hydrogenation reaction between \*N<sub>2</sub> and H<sup>+</sup> can either generate the \*NNH intermediate as discussed above or form the \*N<sub>2</sub> + \*H intermediate through H<sup>+</sup> directly adsorbing onto another active site. To determine the more feasible intermediate, we compared the free energy changes of these two intermediates formed on these four catalysts (Table S3). The results show that all four catalysts are more likely to form \*NNH. Therefore, these five catalysts ( $MM'@N_4O_2-G$ ,  $MM' = \text{MoFe, MoMn, MoCo, MoCr, and VV}$ ) exhibit good selectivity and hold potential as catalysts for the NRR.

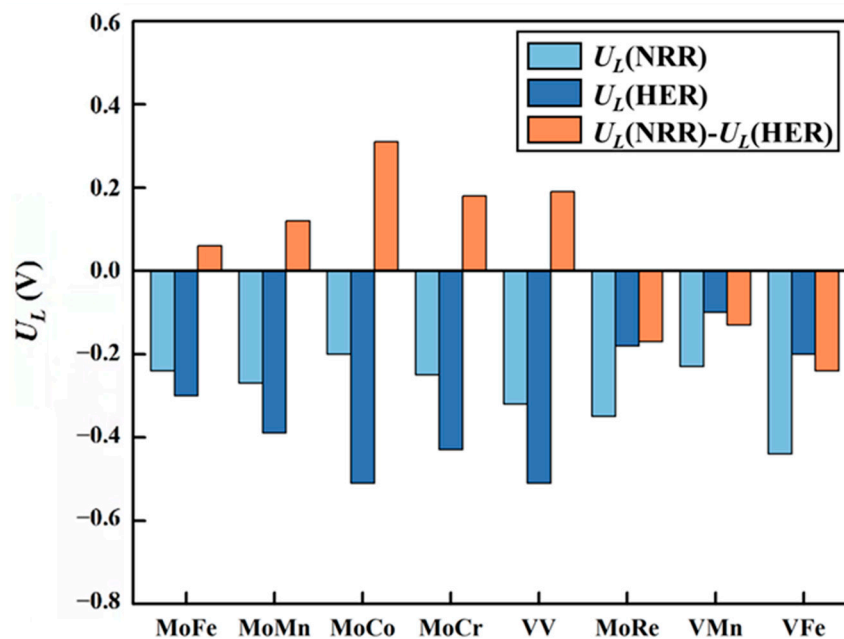


**Figure 11.** Difference between the limiting potential of NRR ( $U_L(\text{NRR})$ ) and the limiting potential of HER ( $U_L(\text{HER})$ ) on the 8 DACs ( $U_L(\text{NRR}) - U_L(\text{HER})$ ).

MoCo@N<sub>4</sub>O<sub>2</sub>-G exhibits the most favorable catalytic performance among the five DACs, with a limiting potential of  $-0.20$  V. Its catalytic activity surpasses that of several other catalysts, including TiV-CG ( $-0.30$  V) [23], FeMo-N<sub>6</sub>-C ( $-0.63$  V) [28], Fe<sub>2</sub>N<sub>4</sub>@graphene ( $-0.32$  V) [29], and Mn<sub>2</sub>ON<sub>5</sub>/G<sup>α</sup> ( $-0.27$  V) [37].

### 3. Computational Methods

All computations in this study, based on spin-polarized density functional theory (DFT) [45,46], were conducted using the Vienna Ab Initio Simulation Package (VASP 5.4.4) [47,48]. The projector augmented wave (PAW) [49] method was employed to deal with the ion–electron interactions. The cutoff energy for the plane-wave basis set was set to 450 eV. The Perdew–Burke–Ernzerhof (PBE) functional [50] within the general gradient approximation (GGA) was used to describe the electronic exchange–correlation interactions. A  $(5 \times 5)$  graphene supercell was adopted as the catalyst substrate, with a vacuum layer of 20 Å introduced along the z-axis to eliminate the interaction between periodic images. For structure optimization and electronic structure calculations, Monkhorst–Pack k-point grids of  $3 \times 3 \times 1$  and  $11 \times 11 \times 1$  were utilized to sample the Brillouin zone. The convergence criteria for energy and forces were set to  $10^{-5}$  eV and 0.02 eV/Å, respectively. To account for van der Waals (vdW) interactions, the DFT-D3 method proposed by Grimme et al. [51] was employed in all calculations. The implicit solvent model implemented in the VASPsol software package (VASPsol 5.4.1) was used to treat the solvation effects [52,53]. To investigate the thermal stability of the DACs, ab initio molecular dynamics (AIMD) simulations [54] were performed for 10 ps at 500 K with a time step of 2 fs.

The Gibbs free energy change ( $\Delta G$ ) for each elementary step of the NRR was calculated using the computational hydrogen electrode (CHE) model proposed by Nørskov et al. [55]. The formula for calculating  $\Delta G$  is as follows:

$$\Delta G = \Delta E + \Delta E_{ZPE} - T\Delta S + neU + \Delta G_{pH}$$

where  $\Delta E$  is the reaction energy of each step calculated by DFT.  $\Delta E_{ZPE}$  and  $\Delta S$  are the changes in zero-point energy and entropy at 298.15 K, respectively, obtained by calculating the vibrational frequencies. The vibrational frequencies and entropy of gas molecules (N<sub>2</sub>, H<sub>2</sub>, NH<sub>3</sub>) are obtained from the NIST database [56].  $U$  represents the electrode potential,

$n$  represents the number of transferred electrons, and  $\Delta G_{pH}$  represents the free energy correction value at pH, defined as  $\Delta G_{pH} = 2.303 \times k_B T \times pH$ . In this work, the pH is set to 0. The highest positive  $\Delta G$  value ( $\Delta G_{\max}$ ) throughout the process was employed to derive the limiting potential ( $U_L$ ), i.e.,  $U_L = -\Delta G_{\max}/e$ .

#### 4. Conclusions

This study systematically explored a range of double-atom catalysts, namely  $MM'@N_4O_2-G$ , for their potential as NRR electrocatalysts using density functional theory. Employing a multi-stage screening strategy, we identified eight candidate catalysts ( $MM'@N_4O_2-G$ ,  $MM' = MoFe, MoCo, MoCr, MoMn, MoRe, VFe, VMn, \text{ and } VV$ ) with both thermodynamic and electrochemical stability among 48 catalysts. The NRR mechanism was extensively studied for these catalysts. Computational results revealed that the NRR on  $VV@N_4O_2-G$  occurs through an enzymatic pathway, while the remaining seven catalysts follow a distal mechanism. Notably, in contrast to other systems,  $MoRe@N_4O_2-G$  facilitates nitrogen reduction by adsorbing two  $N_2$  molecules onto its surface, each anchored to a metal center. Further analysis of the electronic structures elucidated an “acceptance–feedback” mechanism between the active sites and  $N_2$  molecules. The limiting potentials for these eight catalysts ranged from  $-0.20$  to  $-0.37$  V. The volcano plot relationship between  $U_L$  and  $\epsilon d$  demonstrated the cooperative effect of two active sites in the DACs on the catalytic performance. Furthermore, we investigated the selectivity of the eight DACs and identified five potential NRR catalysts ( $MM'@N_4O_2-G$ ,  $MM' = MoFe, MoCo, MoCr, MoMn, \text{ and } VV$ ).  $MoCo@N_4O_2-G$  exhibits the most favorable catalytic performance among the five DACs, with a limiting potential of  $-0.20$  V. AIMD simulations revealed the high thermal stability of these potential NRR catalysts at 500 K, suggesting feasibility for experimental synthesis and practical applications. We hope that this study will drive the exploration of the potential application of DACs in the NRR and other electrochemical reactions.

**Supplementary Materials:** The following supporting information can be downloaded at: <https://www.mdpi.com/article/10.3390/molecules29040779/s1>, Table S1: Number of electrons transferred from  $MM'$  to the  $N_4O_2-G$  carrier ( $Q$  in e). Table S2: Comparison of Gibbs free energy changes for  $*N_2 + N_2(g) \rightarrow *N_2 + *N_2$  and  $*N_2 + *N_2 + H^+ + e^- \rightarrow *NNH + *N_2$  on seven heteronuclear DACs. Table S3: Comparison of Gibbs free energy changes for  $*N_2 + H^+ + e^- \rightarrow *N_2 + *H$  and  $*N_2 + H^+ + e^- \rightarrow *NNH$ . Figure S1: Total energy variation of  $MM'@N_4O_2-G$  ( $MM' = MoCo, MoMn, MoRe, MoCr, VV, VMn, \text{ and } VFe$ ) for 10 ps AIMD simulations at 500 K. Figure S2: Gibbs free energy diagrams of NRR on  $VFe@N_4O_2-G$ . Figure S3: Gibbs free energy diagrams of NRR on  $MoCr@N_4O_2-G, MoMn@N_4O_2-G, \text{ and } VMn@N_4O_2-G$ . Figure S4: PDOS after  $N_2$  adsorption on  $MM'@N_4O_2-G$  ( $MM' = MoFe, MoCr, MoRe, MoMn, VFe, VMn, \text{ and } VV$ ).

**Author Contributions:** Conceptualization, H.D.; methodology, H.D. and H.S.; software, S.L.; validation, H.D., G.X. and H.S.; data curation, H.D.; writing—original draft preparation, H.D.; writing—review and editing, J.L. and X.D.; supervision, J.L.; project administration, J.L.; funding acquisition, J.L. All authors have read and agreed to the published version of the manuscript.

**Funding:** This work was supported by the National Key Research and Development Program of China (Grant No. 2021YFA1500403).

**Institutional Review Board Statement:** Not applicable.

**Informed Consent Statement:** Not applicable.

**Data Availability Statement:** Data are contained within the article and Supplementary Materials.

**Conflicts of Interest:** The authors declare no conflicts of interest.

#### References

1. Suryanto, B.H.R.; Matuszek, K.; Choi, J.; Hodgetts, R.Y.; Du, H.-L.; Bakker, J.M.; Kang, C.S.M.; Cherepanov, P.V.; Simonov, A.N.; MacFarlane, D.R. Nitrogen reduction to ammonia at high efficiency and rates based on a phosphonium proton shuttle. *Science* **2021**, *372*, 1187–1191. [CrossRef] [PubMed]
2. Guo, J.; Chen, P. Catalyst:  $NH_3$  as an Energy Carrier. *Chem* **2017**, *3*, 709–712. [CrossRef]

3. Chen, J.G.; Crooks, R.M.; Seefeldt, L.C.; Bren, K.L.; Bullock, R.M.; Darensbourg, M.Y.; Holland, P.L.; Hoffman, B.; Janik, M.J.; Jones, A.K.; et al. Beyond fossil fuel-driven nitrogen transformations. *Science* **2018**, *360*, eaar6611. [[CrossRef](#)]
4. Rafiqul, I.; Weber, C.; Lehmann, B.; Voss, A. Energy efficiency improvements in ammonia production-perspectives and uncertainties. *Energy* **2005**, *30*, 2487–2504. [[CrossRef](#)]
5. Li, K.; Andersen, S.Z.; Statt, M.J.; Saccoccio, M.; Bukas, V.J.; Krempel, K.; Sažinas, R.; Pedersen, J.B.; Shadravan, V.; Zhou, Y.; et al. Enhancement of lithium-mediated ammonia synthesis by addition of oxygen. *Science* **2021**, *374*, 1593–1597. [[CrossRef](#)]
6. Foster, S.L.; Bakovic, S.I.P.; Duda, R.D.; Maheshwari, S.; Milton, R.D.; Minteer, S.D.; Janik, M.J.; Renner, J.N.; Greenlee, L.F. Catalysts for nitrogen reduction to ammonia. *Nat. Catal.* **2018**, *1*, 490–500. [[CrossRef](#)]
7. Li, S.; Wang, Y.; Du, Y.; Zhu, X.D.; Gao, J.; Zhang, Y.C.; Wu, G. P-Block Metal-Based Electrocatalysts for Nitrogen Reduction to Ammonia: A Minireview. *Small* **2023**, *19*, 16. [[CrossRef](#)]
8. Tang, X.; Wei, Z.; Liu, Q.; Ma, J. Strain engineering the D-band center for Janus MoSSe edge: Nitrogen fixation. *J. Energy Chem.* **2019**, *33*, 155–159. [[CrossRef](#)]
9. Wang, C.; Shan, Y.-T.; Zheng, W.-H.; Zhang, M.; Su, Z.-M. Two-dimensional graphdiyne analogue containing Mo-coordinated porphyrin covalent organic framework as a high-performance electrocatalyst for nitrogen fixation. *Appl. Surf. Sci.* **2022**, *580*, 152359. [[CrossRef](#)]
10. Yang, X.; An, P.; Wang, R.; Jia, J. Tuning the Site-to-Site Interaction of Heteronuclear Diatom Catalysts MoTM/C<sub>2</sub>N (TM = 3d Transition Metal) for Electrochemical Ammonia Synthesis. *Molecules* **2023**, *28*, 4003. [[CrossRef](#)]
11. He, C.; Wang, R.; Xiang, D.; Li, X.; Fu, L.; Jian, Z.; Huo, J.; Li, S. Charge-regulated CO<sub>2</sub> capture capacity of metal atom embedded graphyne: A first-principles study. *Appl. Surf. Sci.* **2020**, *509*, 145392. [[CrossRef](#)]
12. Lang, R.; Xi, W.; Liu, J.-C.; Cui, Y.-T.; Li, T.; Lee, A.F.; Chen, F.; Chen, Y.; Li, L.; Li, L.; et al. Non defect-stabilized thermally stable single-atom catalyst. *Nat. Commun.* **2019**, *10*, 234. [[CrossRef](#)]
13. Li, F.; Liu, X.; Chen, Z. 1 + 1' > 2: Heteronuclear Biatom Catalyst Outperforms Its Homonuclear Counterparts for CO Oxidation. *Small Methods* **2019**, *3*, 1800480. [[CrossRef](#)]
14. Song, W.; Fu, Z.; Liu, X.; Guo, Y.; He, C.; Fu, L. Density functional theory study of a two-atom active site transition-metal/iridium electrocatalyst for ammonia synthesis. *J. Mater. Chem. A* **2022**, *10*, 13946–13957. [[CrossRef](#)]
15. Wu, J.; Li, J.-H.; Yu, Y.-X. Single Nb or W Atom-Embedded BP Monolayers as Highly Selective and Stable Electrocatalysts for Nitrogen Fixation with Low-Onset Potentials. *ACS Appl. Mater. Interfaces* **2021**, *13*, 10026–10036. [[CrossRef](#)]
16. Wang, Y.; Liu, Y.; Liu, W.; Wu, J.; Li, Q.; Feng, Q.; Chen, Z.; Xiong, X.; Wang, D.; Lei, Y. Regulating the coordination structure of metal single atoms for efficient electrocatalytic CO<sub>2</sub> reduction. *Energy Environ. Sci.* **2020**, *13*, 4609–4624. [[CrossRef](#)]
17. Mannix, A.J.; Zhou, X.-F.; Kiraly, B.; Wood, J.D.; Alducin, D.; Myers, B.D.; Liu, X.; Fisher, B.L.; Santiago, U.; Guest, J.R.; et al. Synthesis of borophenes: Anisotropic, two-dimensional boron polymorphs. *Science* **2015**, *350*, 1513–1516. [[CrossRef](#)] [[PubMed](#)]
18. Guo, R.; Hu, M.; Zhang, W.; He, J. Boosting Electrochemical Nitrogen Reduction Performance over Binuclear Mo Atoms on N-Doped Nanoporous Graphene: A Theoretical Investigation. *Molecules* **2019**, *24*, 1777. [[CrossRef](#)]
19. Xie, Y.; Chen, X.; Sun, K.; Zhang, J.; Lai, W.H.; Liu, H.; Wang, G. Direct Oxygen-Oxygen Cleavage through Optimizing Interatomic Distances in Dual Single-atom Electrocatalysts for Efficient Oxygen Reduction Reaction. *Angew. Chem. Int. Ed.* **2023**, *62*, e202301833. [[CrossRef](#)]
20. Liu, C.; Zheng, H.; Wang, T.; Guo, Z.; Zhu, F.; Xie, H.; Qin, G.; Li, H.; Li, S. The role of single-boron of N-doped graphene for effective nitrogen reduction. *J. Mater. Sci. Technol.* **2023**, *159*, 244–250. [[CrossRef](#)]
21. Orek, C.; Bartolomei, M.; Coletti, C.; Bulut, N. Graphene as Nanocarrier for Gold(I)-Monocarbene Complexes: Strength and Nature of Physisorption. *Molecules* **2023**, *28*, 3941. [[CrossRef](#)]
22. Wang, X.; Niu, H.; Wan, X.; Wang, J.; Kuai, C.; Zhang, Z.; Guo, Y. Identifying TM-N<sub>4</sub> active sites for selective CO<sub>2</sub>-to-CH<sub>4</sub> conversion: A computational study. *Appl. Surf. Sci.* **2022**, *582*, 152470. [[CrossRef](#)]
23. Hu, R.; Li, Y.; Zeng, Q.; Wang, F.; Shang, J. Bimetallic Pairs Supported on Graphene as Efficient Electrocatalysts for Nitrogen Fixation: Search for the Optimal Coordination Atoms. *ChemSusChem* **2020**, *13*, 3636–3644. [[CrossRef](#)] [[PubMed](#)]
24. Li, X.; Rong, H.; Zhang, J.; Wang, D.; Li, Y. Modulating the local coordination environment of single-atom catalysts for enhanced catalytic performance. *Nano Res.* **2020**, *13*, 1842–1855. [[CrossRef](#)]
25. Zhang, J.; Yang, H.; Liu, B. Coordination Engineering of Single-Atom Catalysts for the Oxygen Reduction Reaction: A Review. *Adv. Energy Mater.* **2020**, *11*, 2002473. [[CrossRef](#)]
26. Qian, Y.; Liu, Y.; Zhao, Y.; Zhang, X.; Yu, G. Single vs double atom catalyst for N<sub>2</sub> activation in nitrogen reduction reaction: A DFT perspective. *EcoMat* **2020**, *2*, e12014. [[CrossRef](#)]
27. Chen, Z.W.; Yan, J.M.; Jiang, Q. Single or Double: Which Is the Altar of Atomic Catalysts for Nitrogen Reduction Reaction? *Small Methods* **2018**, *3*, 1800291. [[CrossRef](#)]
28. Gao, S.; Liu, X.; Wang, Z.; Lu, Y.; Sa, R.; Li, Q.; Sun, C.; Chen, X.; Ma, Z. Spin regulation for efficient electrocatalytic N<sub>2</sub> reduction over diatomic Fe-Mo catalyst. *J. Colloid Interface Sci.* **2023**, *630*, 215–223. [[CrossRef](#)] [[PubMed](#)]
29. Zhang, Z.; Huang, X.; Xu, H. Anchoring an Fe Dimer on Nitrogen-Doped Graphene toward Highly Efficient Electrocatalytic Ammonia Synthesis. *ACS Appl. Mater. Interfaces* **2021**, *13*, 43632–43640. [[CrossRef](#)]
30. Han, S.; Song, R.; Wang, M.; Gong, Q.; Xiong, J.; Xu, Z. Electrocatalytic reduction of N<sub>2</sub> on FeRu dual-atom catalyst anchored in N-doped phosphorene. *Mol. Catal.* **2023**, *539*, 113032. [[CrossRef](#)]

31. Jiang, Q.; Meng, Y.; Li, K.; Wang, Y.; Wu, Z. Theoretical insights into bimetallic atoms supported on PC<sub>6</sub> as highly efficient electrocatalysts for N<sub>2</sub> electroreduction to NH<sub>3</sub>. *Appl. Surf. Sci.* **2021**, *547*, 149208. [CrossRef]
32. Skúlason, E.; Bligaard, T.; Gudmundsdóttir, S.; Studt, F.; Rossmeisl, J.; Abild-Pedersen, F.; Vegge, T.; Jónsson, H.; Nørskov, J.K. A theoretical evaluation of possible transition metal electro-catalysts for N<sub>2</sub> reduction. *Phys. Chem. Chem. Phys.* **2012**, *14*, 1235–1245. [CrossRef] [PubMed]
33. Guo, X.; Gu, J.; Lin, S.; Zhang, S.; Chen, Z.; Huang, S. Tackling the Activity and Selectivity Challenges of Electrocatalysts toward the Nitrogen Reduction Reaction via Atomically Dispersed Biatom Catalysts. *J. Am. Chem. Soc.* **2020**, *142*, 5709–5721. [CrossRef]
34. Han, L.; Liu, X.; Chen, J.; Lin, R.; Liu, H.; Lü, F.; Bak, S.; Liang, Z.; Zhao, S.; Stavitski, E.; et al. Atomically Dispersed Molybdenum Catalysts for Efficient Ambient Nitrogen Fixation. *Angew. Chem. Int. Ed.* **2019**, *58*, 2321–2325. [CrossRef]
35. Han, X.-Q.; Lang, Z.-L.; Zhang, F.-Y.; Xu, H.-L.; Su, Z.-M. Computational evaluation of FeMo heteroatom coeffect induced high electroreduction activity of N<sub>2</sub>-to-NH<sub>3</sub>. *Appl. Surf. Sci.* **2022**, *579*, 152214. [CrossRef]
36. Shang, H.; Zhou, X.; Dong, J.; Li, A.; Zhao, X.; Liu, Q.; Lin, Y.; Pei, J.; Li, Z.; Jiang, Z.; et al. Engineering unsymmetrically coordinated Cu-S<sub>1</sub>N<sub>3</sub> single atom sites with enhanced oxygen reduction activity. *Nat. Commun.* **2020**, *11*, 3049. [CrossRef] [PubMed]
37. Wu, J.; Wu, D.; Li, H.; Song, Y.; Lv, W.; Yu, X.; Ma, D. Tailoring the coordination environment of double-atom catalysts to boost electrocatalytic nitrogen reduction: A first-principles study. *Nanoscale* **2023**, *15*, 16056–16067. [CrossRef]
38. Wang, S.; Shi, L.; Bai, X.; Li, Q.; Ling, C.; Wang, J. Highly Efficient Photo-/Electrocatalytic Reduction of Nitrogen into Ammonia by Dual-Metal Sites. *ACS Cent. Sci.* **2020**, *6*, 1762–1771. [CrossRef]
39. Zhang, Y.-X.; Zhang, S.; Huang, H.; Liu, X.; Li, B.; Lee, Y.; Wang, X.; Bai, Y.; Sun, M.; Wu, Y.; et al. General Synthesis of a Diatomic Catalyst Library via a Macrocyclic Precursor-Mediated Approach. *J. Am. Chem. Soc.* **2023**, *145*, 4819–4827. [CrossRef] [PubMed]
40. Zafari, M.; Nissimagoudar, A.S.; Umer, M.; Lee, G.; Kim, K.S. First principles and machine learning based superior catalytic activities and selectivities for N<sub>2</sub> reduction in MBenes, defective 2D materials and 2D  $\pi$ -conjugated polymer-supported single atom catalysts. *J. Mater. Chem. A* **2021**, *9*, 9203–9213. [CrossRef]
41. Ling, C.; Ouyang, Y.; Li, Q.; Bai, X.; Mao, X.; Du, A.; Wang, J. A General Two-Step Strategy-Based High-Throughput Screening of Single Atom Catalysts for Nitrogen Fixation. *Small Methods* **2018**, *3*, 1800376. [CrossRef]
42. Chun, H.-J.; Apaja, V.; Clayborne, A.; Honkala, K.; Greeley, J. Atomistic Insights into Nitrogen-Cycle Electrochemistry: A Combined DFT and Kinetic Monte Carlo Analysis of NO Electrochemical Reduction on Pt(100). *ACS Catal.* **2017**, *7*, 3869–3882. [CrossRef]
43. Liu, C.; Li, Q.; Wu, C.; Zhang, J.; Jin, Y.; MacFarlane, D.R.; Sun, C. Single-Boron Catalysts for Nitrogen Reduction Reaction. *J. Am. Chem. Soc.* **2019**, *141*, 2884–2888. [CrossRef]
44. Qi, J.; Gao, L.; Wei, F.; Wan, Q.; Lin, S. Design of a High-Performance Electrocatalyst for N<sub>2</sub> Conversion to NH<sub>3</sub> by Trapping Single Metal Atoms on Stepped CeO<sub>2</sub>. *ACS Appl. Mater. Interfaces* **2019**, *11*, 47525–47534. [CrossRef]
45. Hohenberg, P.; Kohn, W. Inhomogeneous Electron Gas. *Phys. Rev.* **1964**, *136*, B864–B871. [CrossRef]
46. Kohn, W.; Sham, L.J. Self-Consistent Equations Including Exchange and Correlation Effects. *Phys. Rev.* **1965**, *140*, A1133–A1138. [CrossRef]
47. Kresse, G.; Furthmüller, J. Efficient iterative schemes for ab initio total-energy calculations using a plane-wave basis set. *Phys. Rev. B* **1996**, *54*, 11169–11186. [CrossRef] [PubMed]
48. Blöchl, P.E. Projector augmented-wave method. *Phys. Rev. B* **1994**, *50*, 17953–17979. [CrossRef] [PubMed]
49. Kresse, G.; Furthmüller, J. Efficiency of ab-initio total energy calculations for metals and semiconductors using a plane-wave basis set. *Comput. Mater. Sci.* **1996**, *6*, 15–50. [CrossRef]
50. Perdew, J.P.; Burke, K.; Ernzerhof, M. Generalized Gradient Approximation Made Simple. *Phys. Rev. Lett.* **1996**, *77*, 3865–3868. [CrossRef] [PubMed]
51. Grimme, S. Semiempirical GGA-type density functional constructed with a long-range dispersion correction. *J. Comput. Chem.* **2006**, *27*, 1787–1799. [CrossRef] [PubMed]
52. Mathew, K.; Sundararaman, R.; Letchworth-Weaver, K.; Arias, T.A.; Hennig, R.G. Implicit solvation model for density-functional study of nanocrystal surfaces and reaction pathways. *J. Chem. Phys.* **2014**, *140*, 084106. [CrossRef]
53. Mathew, K.; Kolluru, V.S.C.; Mula, S.; Steinmann, S.N.; Hennig, R.G. Implicit self-consistent electrolyte model in plane-wave density-functional theory. *J. Chem. Phys.* **2019**, *151*, 234101. [CrossRef]
54. Barnett, R.N.; Landman, U. AIMD-Born-Oppenheimer molecular-dynamics simulations of finite systems: Structure and dynamics of (H<sub>2</sub>O)<sub>2</sub>. *Phys. Rev. B* **1993**, *48*, 2081–2097. [CrossRef] [PubMed]
55. Nørskov, J.K.; Rossmeisl, J.; Logadottir, A.; Lindqvist, L.; Kitchin, J.R.; Bligaard, T.; Jónsson, H. Origin of the Overpotential for Oxygen Reduction at a Fuel-Cell Cathode. *J. Phys. Chem. B* **2004**, *108*, 17886–17892. [CrossRef]
56. The National Institute of Standards and Technology (NIST). Available online: <http://cccbdb.nist.gov/> (accessed on 12 June 2023).

**Disclaimer/Publisher’s Note:** The statements, opinions and data contained in all publications are solely those of the individual author(s) and contributor(s) and not of MDPI and/or the editor(s). MDPI and/or the editor(s) disclaim responsibility for any injury to people or property resulting from any ideas, methods, instructions or products referred to in the content.